Supporting Information

Aluminum Nanotripods for Light-Matter Coupling Robust to Nanoemitter Orientation

Víctor Pacheco-Peña[1,2], Antonio I. Fernández-Domínguez[3], Yu Luo[4], Miguel Beruete[1,5] and Miguel Navarro-Cía[6,]*

*Corresponding Author: E-mail: m.navarro-cia@bham.ac.uk

[1]Antennas Group−TERALAB, Universidad Pública de Navarra, Pamplona 31006, Spain
[2]Department of Electrical and Systems Engineering, University of Pennsylvania, Philadelphia, PA 19104, USA
[3]Departamento de Física Teórica de la Materia Condensada and Condensed Matter Physics Center (IFIMAC), Universidad Autónoma de Madrid, Madrid 28049, Spain
[4]School of Electrical & Electronic Engineering, Nanyang Technological University, Singapore 639798, Singapore
[5]Institute of Smart Cities, Universidad Pública de Navarra, Pamplona 31006, Spain
[6]School of Physics and Astronomy, University of Birmingham, Birmingham B15 2TT, U.K.

Multislab geometry mimicking the nanotripod

In this section, the transformed multislab (or comb) geometry shown in Figure 1b, and reproduced again here as Figure S1, is solved.
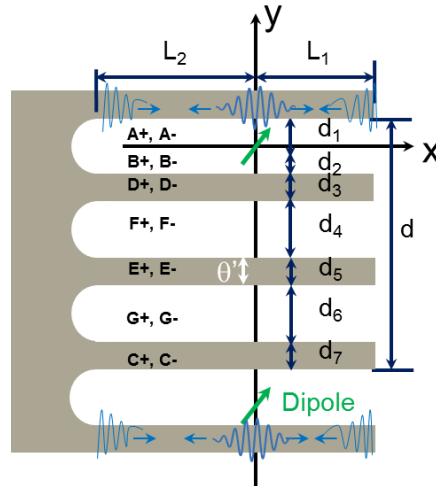

Figure S1. Sketch of the transformed scenario, an Al comb, along with the relevant coefficients and geometrical parameters.

Considering that the total diameter of the Al nanotripod is sufficiently smaller than the operational wavelength ($l' \ll \lambda_0$), the near-field approximation can be used. Thus, the electric field can be fully described by an electrostatic potential satisfying Laplace's equation. In the multislab geometry shown in Figure 1b, it is possible to excite surface plasmon modes in both transversal and longitudinal directions, with their propagation along the x- and y- axis, respectively. However, we are interested in deriving the surface plasmon modes excited in the comb geometry when $L_1 + L_2 \gg \theta$, thereby, the contribution of the longitudinal LSP modes (i.e., those with phase variation along y) can be neglected and one can assume that the excited LSP modes are mainly due to the transversal modes (i.e., those with phase variation along x). With this in mind, the electrostatic potentials outside and inside the metal strips in Figure 1b can be calculated as a sum of all discrete transverse modes, as follows:

$$\sum_k \left[\frac{1}{1+e^{2ik(L_1+L_2)+i\Delta\varphi_1+i\Delta\varphi_2}} \left(e^{ikx}+e^{-ikx+2ikL_1+i\Delta\varphi_1}\right)\left(A_+e^{-ky}+B_+e^{-ky}+B_-e^{ky}\right) \right], 0<y<d_1 \tag{S1}$$

$$\sum_k \left[\frac{1}{1+e^{2ik(L_1+L_2)+i\Delta\varphi_1+i\Delta\varphi_2}} \left(e^{ikx}+e^{-ikx+2ikL_1+i\Delta\varphi_1}\right)\left(A_-e^{ky}+B_+e^{-ky}+B_-e^{ky}\right) \right], -d_2<y<0 \tag{S2}$$

$$\sum_k \left[\frac{1}{1+e^{2ik(L_1+L_2)+i\Delta\varphi_1+i\Delta\varphi_2}} \left(e^{ikx}+e^{-ikx+2ikL_1+i\Delta\varphi_1}\right)\left(F_+e^{-ky}+F_-e^{ky}\right) \right], -(d_2+d_3+d_4)<y<-(d_2+d_3) \tag{S3}$$

$$\sum_k \left[\frac{1}{1+e^{2ik(L_1+L_2)+i\Delta\varphi_1+i\Delta\varphi_2}} \left(e^{ikx}+e^{-ikx+2ikL_1+i\Delta\varphi_1}\right)\left(G_+e^{-ky}+G_-e^{ky}\right) \right], y\begin{cases}>-(d_2+d_3+d_4+d_5+d_6)\\<-(d_1+2d_2+d_3)\end{cases} \tag{S4}$$

$$\sum_k \left[\frac{1}{1+e^{2ik(L_1+L_2)+i\Delta\varphi_1+i\Delta\varphi_2}} \left(e^{ikx}+e^{-ikx+2ikL_1+i\Delta\varphi_1}\right)\left(D_+e^{-ky}+D_-e^{ky}\right) \right], -(d_2+d_3)<y<-d_2 \tag{S5}$$

$$\sum_k \left[\frac{1}{1+e^{2ik(L_1+L_2)+i\Delta\varphi_1+i\Delta\varphi_2}} \left(e^{ikx}+e^{-ikx+2ikL_1+i\Delta\varphi_1}\right)\left(E_+e^{-ky}+E_-e^{ky}\right) \right], y\begin{cases}>-(d_2+d_3+d_4+d_5)\\<-(d_2+d_3+d_4)\end{cases} \tag{S6}$$

$$\sum_k \left[\frac{1}{1+e^{2ik(L_1+L_2)+i\Delta\varphi_1+i\Delta\varphi_2}} \left(e^{ikx}+e^{-ikx+2ikL_1+i\Delta\varphi_1}\right)\left(C_+e^{-ky}+C_-e^{ky}\right) \right], y\begin{cases}>-(d_2+d_3+d_4+d_5+d_6+d_7)\\<-(d_2+d_3+d_4+d_5+d_6)\end{cases} \tag{S7}$$

where A+ and A- are the expansion coefficients of the incident potential, B_+ and B. are the coefficients related to the scattering potential in the region where the dipole is placed ($d_2<y<d_1$), F_+, F., G_+ and G. are the coefficients associated to the scattering potential in the region where a dipole is absent (d_4 and d_6) and C_+, C., D_+, D., E_+ and E. are those corresponding to the potential inside the metal strips (d_7, d_3 and d_5, respectively). The wave vector k and the coefficients A_+ and A. are defined as follows:

$$k = \frac{n\pi - \tfrac{1}{2}\Delta\varphi_1 - \tfrac{1}{2}\Delta\varphi_2}{L_1+L_2} \tag{S8}$$

$$A\pm = \frac{\pm p_y - ip_x\,\mathrm{sgn}(k)}{2\varepsilon_0} \tag{S9}$$

where $\Delta\varphi_1$ and $\Delta\varphi_2$ are the correction of phase applied to the nanotripod to take into account the complex reflection experienced by the surface plasmon waves at the extremes of the nanoparticle (right and left sides of the transformed geometry, respectively), p_y and p_x are the

components of the dipole moment along the x and y directions, respectively, and ε_0 is the permittivity in vacuum. The other eight unknown coefficients B$_+$, B$_-$, C$_+$, C$_-$, D$_+$, D$_-$, E$_+$ and E$_-$ can be solved by applying boundary conditions at each interface of Figure 1b. First, the condition of conservation of the parallel component of the electric field at the boundaries d_1 ($= -(d_2 + d_3 + d_4 + d_5 + d_6 + d_7)$), $-d_2$, $-(d_2 + d_3)$, $-(d_2 + d_3 + d_4)$, $-(d_2 + d_3 + d_4 + d_5)$, and $-(d_2 + d_3 + d_4 + d_5 + d_6)$ is applied, as follows:

$$A_- e^{-kd_2} + B_+ e^{kd_2} + B_- e^{-kd_2} = D_- e^{-kd_2} + D_+ e^{kd_2} \tag{S10}$$

$$F_+ e^{k(d_2+d_3)} + F_- e^{-k(d_2+d_3)} = D_- e^{-k(d_2+d_3)} + D_+ e^{k(d_2+d_3)} \tag{S11}$$

$$F_+ e^{k(d_2+d_3+d_4)} + F_- e^{-k(d_2+d_3+d_4)} = E_- e^{-k(d_2+d_3+d_4)} + E_+ e^{k(d_2+d_3+d_4)} \tag{S12}$$

$$G_+ e^{k(d_2+d_3+d_4+d_5)} + G_- e^{-k(d_2+d_3+d_4+d_5)} = E_- e^{-k(d_2+d_3+d_4+d_5)} + E_+ e^{k(d_2+d_3+d_4+d_5)} \tag{S13}$$

$$A_+ e^{-kd_1} + B_+ e^{-kd_1} + B_- e^{kd_1} = C_- e^{-k(d_2+d_3+d_4+d_5+d_6+d_7)} + C_+ e^{k(d_2+d_3+d_4+d_5+d_6+d_7)} \tag{S14}$$

$$G_+ e^{k(d_2+d_3+d_4+d_5+d_6)} + G_- e^{-k(d_2+d_3+d_4+d_5+d_6)} = C_- e^{-k(d_2+d_3+d_4+d_5+d_6)} + C_+ e^{k(d_2+d_3+d_4+d_5+d_6)} \tag{S15}$$

Also, the condition of conservation of the normal component of the displacement field at the same boundaries as the above equations is applied:

$$A_- e^{-kd_2} - B_+ e^{kd_2} + B_- e^{-kd_2} = \varepsilon D_- e^{-kd_2} - \varepsilon D_+ e^{kd_2} \tag{S16}$$

$$F_+ e^{k(d_2+d_3)} - F_- e^{-k(d_2+d_3)} = -\varepsilon D_- e^{-k(d_2+d_3)} + \varepsilon D_+ e^{k(d_2+d_3)} \tag{S17}$$

$$-F_+ e^{k(d_2+d_3+d_4)} + F_- e^{-k(d_2+d_3+d_4)} = \varepsilon E_- e^{-k(d_2+d_3+d_4)} - \varepsilon E_+ e^{k(d_2+d_3+d_4)} \tag{S18}$$

$$G_+ e^{k(d_2+d_3+d_4+d_5)} + G_- e^{-k(d_2+d_3+d_4+d_5)} = E_- e^{-k(d_2+d_3+d_4+d_5)} + E_+ e^{k(d_2+d_3+d_4+d_5)} \tag{S19}$$

$$A_+ e^{-kd_1} + B_+ e^{-kd_1} - B_- e^{kd_1} = -\varepsilon C_- e^{-k(d_2+d_3+d_4+d_5+d_6+d_7)} + \varepsilon C_+ e^{k(d_2+d_3+d_4+d_5+d_6+d_7)} \tag{S20}$$

$$-G_+ e^{k(d_2+d_3+d_4+d_5+d_6)} + G_- e^{-k(d_2+d_3+d_4+d_5+d_6)} = \varepsilon C_- e^{-k(d_2+d_3+d_4+d_5+d_6)} - \varepsilon C_+ e^{k(d_2+d_3+d_4+d_5+d_6)} \tag{S21}$$

The solutions of the potentials in the real space for the region where there is $(-d_2 < y < d_1)$ and there is not a dipole (d_4, d_6), ϕ_1^s, ϕ_2^s and ϕ_3^s, respectively, can be then obtained by applying an inverse Fourier Transform to the induced potentials:

$$\phi_1^s = \frac{1}{2\varepsilon_0(L_1+L_2)}\sum_n\left\langle\left\{\begin{array}{l}p_x[\sin(kx)-\sin(kx-2kL_1-\Delta\varphi_1)]+\\p_y[\cos(kx)+\cos(kx-2kL_1-\Delta\varphi_1)]\end{array}\right\}(B_+e^{-ky}+B_-e^{ky})\right\rangle \quad (S22)$$

$$\phi_2^s = \frac{1}{2\varepsilon_0(L_1+L_2)}\sum_n\left\langle\left\{\begin{array}{l}p_x[\sin(kx)-\sin(kx-2kL_1-\Delta\varphi_1)]+\\p_y[\cos(kx)+\cos(kx-2kL_1-\Delta\varphi_1)]\end{array}\right\}(F_+e^{-ky}+F_-e^{ky})\right\rangle \quad (S23)$$

$$\phi_3^s = \frac{1}{2\varepsilon_0(L_1+L_2)}\sum_n\left\langle\left\{\begin{array}{l}p_x[\sin(kx)-\sin(kx-2kL_1-\Delta\varphi_1)]+\\p_y[\cos(kx)+\cos(kx-2kL_1-\Delta\varphi_1)]\end{array}\right\}(G_+e^{-ky}+G_-e^{ky})\right\rangle \quad (S24)$$

Following the same procedure, the potentials inside the three metallic slabs (ϕ_1^m, ϕ_2^m and ϕ_3^m) are:

$$\phi_1^m = \frac{1}{2\varepsilon_0(L_1+L_2)}\sum_n\left\langle\left\{\begin{array}{l}p_x[\sin(kx)-\sin(kx-2kL_1-\Delta\varphi_1)]+\\p_y[\cos(kx)+\cos(kx-2kL_1-\Delta\varphi_1)]\end{array}\right\}(C_+e^{-ky}+C_-e^{ky})\right\rangle \quad (S25)$$

$$\phi_2^m = \frac{1}{2\varepsilon_0(L_1+L_2)}\sum_n\left\langle\left\{\begin{array}{l}p_x[\sin(kx)-\sin(kx-2kL_1-\Delta\varphi_1)]+\\p_y[\cos(kx)+\cos(kx-2kL_1-\Delta\varphi_1)]\end{array}\right\}(D_+e^{-ky}+D_-e^{ky})\right\rangle \quad (S26)$$

$$\phi_3^m = \frac{1}{2\varepsilon_0(L_1+L_2)}\sum_n\left\langle\left\{\begin{array}{l}p_x[\sin(kx)-\sin(kx-2kL_1-\Delta\varphi_1)]+\\p_y[\cos(kx)+\cos(kx-2kL_1-\Delta\varphi_1)]\end{array}\right\}(E_+e^{-ky}+E_-e^{ky})\right\rangle \quad (S27)$$

Finally, by differentiating the potentials of each region, the x and y components of the electric field can be calculated, as follows:

$$E_{1x}^s = \sum_n -\frac{k}{2\varepsilon_0(L_1+L_2)}\left\langle\left\{\begin{array}{l}p_x[\cos(kx)-\cos(kx-2kL_1-\Delta\varphi_1)]\\-p_y[\sin(kx)+\sin(kx-2kL_1-\Delta\varphi_1)]\end{array}\right\}(B_+e^{-ky}+B_-e^{ky})\right\rangle \quad (S28)$$

$$E_{2x}^s = \sum_n -\frac{k}{2\varepsilon_0(L_1+L_2)}\left\langle\left\{\begin{array}{l}p_x[\cos(kx)-\cos(kx-2kL_1-\Delta\varphi_1)]\\-p_y[\sin(kx)+\sin(kx-2kL_1-\Delta\varphi_1)]\end{array}\right\}(F_+e^{-ky}+F_-e^{ky})\right\rangle \quad (S29)$$

$$E_{3x}^s = \sum_n -\frac{k}{2\varepsilon_0(L_1+L_2)}\left\langle \left\{ \begin{matrix} p_x[\cos(kx)-\cos(kx-2kL_1-\Delta\varphi_1)] \\ -p_y[\sin(kx)+\sin(kx-2kL_1-\Delta\varphi_1)] \end{matrix} \right\} (G_+e^{-ky}+G_-e^{ky}) \right\rangle \quad \text{(S30)}$$

$$E_{1x}^m = \sum_n -\frac{k}{2\varepsilon_0(L_1+L_2)}\left\langle \left\{ \begin{matrix} p_x[\cos(kx)-\cos(kx-2kL_1-\Delta\varphi_1)] \\ -p_y[\sin(kx)+\sin(kx-2kL_1-\Delta\varphi_1)] \end{matrix} \right\} (C_+e^{-ky}+C_-e^{ky}) \right\rangle \quad \text{(S31)}$$

$$E_{2x}^m = \sum_n -\frac{k}{2\varepsilon_0(L_1+L_2)}\left\langle \left\{ \begin{matrix} p_x[\cos(kx)-\cos(kx-2kL_1-\Delta\varphi_1)] \\ -p_y[\sin(kx)+\sin(kx-2kL_1-\Delta\varphi_1)] \end{matrix} \right\} (D_+e^{-ky}+D_-e^{ky}) \right\rangle \quad \text{(S32)}$$

$$E_{3x}^m = \sum_n -\frac{k}{2\varepsilon_0(L_1+L_2)}\left\langle \left\{ \begin{matrix} p_x[\cos(kx)-\cos(kx-2kL_1-\Delta\varphi_1)] \\ -p_y[\sin(kx)+\sin(kx-2kL_1-\Delta\varphi_1)] \end{matrix} \right\} (E_+e^{-ky}+E_-e^{ky}) \right\rangle \quad \text{(S33)}$$

$$E_{1y}^s = \sum_n -\frac{k}{2\varepsilon_0(L_1+L_2)}\left\langle \left\{ \begin{matrix} p_x[\sin(kx)-\sin(kx-2kL_1-\Delta\varphi_1)]+ \\ p_y[\cos(kx)+\cos(kx-2kL_1-\Delta\varphi_1)] \end{matrix} \right\} (-B_+e^{-ky}+B_-e^{ky}) \right\rangle \quad \text{(S34)}$$

$$E_{2y}^s = \sum_n -\frac{k}{2\varepsilon_0(L_1+L_2)}\left\langle \left\{ \begin{matrix} p_x[\sin(kx)-\sin(kx-2kL_1-\Delta\varphi_1)]+ \\ p_y[\cos(kx)+\cos(kx-2kL_1-\Delta\varphi_1)] \end{matrix} \right\} (-F_+e^{-ky}+F_-e^{ky}) \right\rangle \quad \text{(S35)}$$

$$E_{3y}^s = \sum_n -\frac{k}{2\varepsilon_0(L_1+L_2)}\left\langle \left\{ \begin{matrix} p_x[\sin(kx)-\sin(kx-2kL_1-\Delta\varphi_1)]+ \\ p_y[\cos(kx)+\cos(kx-2kL_1-\Delta\varphi_1)] \end{matrix} \right\} (-G_+e^{-ky}+G_-e^{ky}) \right\rangle \quad \text{(S36)}$$

$$E_{1y}^m = \sum_n -\frac{k}{2\varepsilon_0(L_1+L_2)}\left\langle \left\{ \begin{matrix} p_x[\sin(kx)-\sin(kx-2kL_1-\Delta\varphi_1)]+ \\ p_y[\cos(kx)+\cos(kx-2kL_1-\Delta\varphi_1)] \end{matrix} \right\} (-C_+e^{-ky}+C_-e^{ky}) \right\rangle \quad \text{(S37)}$$

$$E_{2y}^m = \sum_n -\frac{k}{2\varepsilon_0(L_1+L_2)}\left\langle \left\{ \begin{matrix} p_x[\sin(kx)-\sin(kx-2kL_1-\Delta\varphi_1)]+ \\ p_y[\cos(kx)+\cos(kx-2kL_1-\Delta\varphi_1)] \end{matrix} \right\} (-D_+e^{-ky}+D_-e^{ky}) \right\rangle \quad \text{(S38)}$$

$$E_{3y}^m = \sum_n -\frac{k}{2\varepsilon_0(L_1+L_2)}\left\langle \left\{ \begin{matrix} p_x[\sin(kx)-\sin(kx-2kL_1-\Delta\varphi_1)]+ \\ p_y[\cos(kx)+\cos(kx-2kL_1-\Delta\varphi_1)] \end{matrix} \right\} (-E_+e^{-ky}+E_-e^{ky}) \right\rangle \quad \text{(S39)}$$

Due to the complexity of each constant, their solutions are not shown here. However, they can be directly obtained manually or using a mathematics software.

The classical line dipole from the original frame is transformed to an array of line dipoles with periodicity 2π in the multislab scenario whose amplitudes depend on the classical line dipole z'-position. The amplitude of the dipoles in the transformed frame as a function of the

classical line dipole *z'*-position is $\bar{p} = \bar{p}'\dfrac{1}{a}$, where *a* denotes the distance from the dipole to

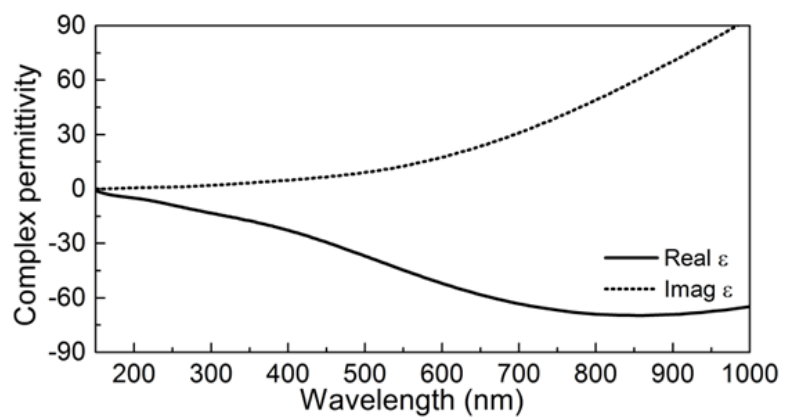the centre of the nanotripod core.

Al model

Figure S2. Aluminum complex permittivity used throughout this manuscript.

Discrete distribution of the LSP modes

Here, we evaluate the influence of θ' to the LSP modes excited in the Al tripods and how they are distributed in the spectrum. The resonant condition can be derived from the formulation shown in section *"Multislab geometry mimicking the nanotripod"* taking into account the condition of divergence of the coefficient of the scattered potential ($B_\pm$). The LSP modes for the smoothly connected nanotripods are distributed at discrete wavelengths following the resonant condition:

$$8e^{(11d_1+21d_2+15d_3)k}\left\{4\varepsilon+(\varepsilon-1)^2\cosh[(d_1+d_2-d_3)k]-(\varepsilon+1)^2\cosh[(d_1+d_2+d_3)k]\right\}$$
$$\times\left\{2\varepsilon-(\varepsilon-1)^2\cosh[(d_1+d_2-d_3)k]+(\varepsilon+1)^2\cosh[(d_1+d_2+d_3)k]\right\}^2=0 \qquad \text{(S40)}$$

where k is defined in Eq. (S8). Here we have considered $d_4 = d_6 = d_1 + d_2$ and $d_5 = d_7 = d_3$ in order to reduce the above expression and simplify its study.
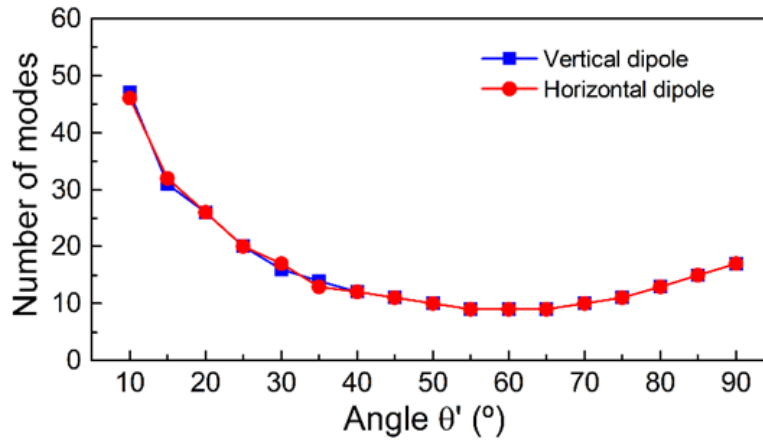

Figure S3. Number of modes as a function of θ' when a vertical (blue) and a horizontal (red) oriented dipole illuminates the nanotripod.

The LSP modes supported by nanotripods with $l' = 16$ nm and different values of θ' are shown in Figure S3 under vertical and horizontal dipole orientations. The number of LSP modes

decreases with θ' until $\theta' \sim 60°$ (condition at which the structure is quasi-self-complementary) and then increases.

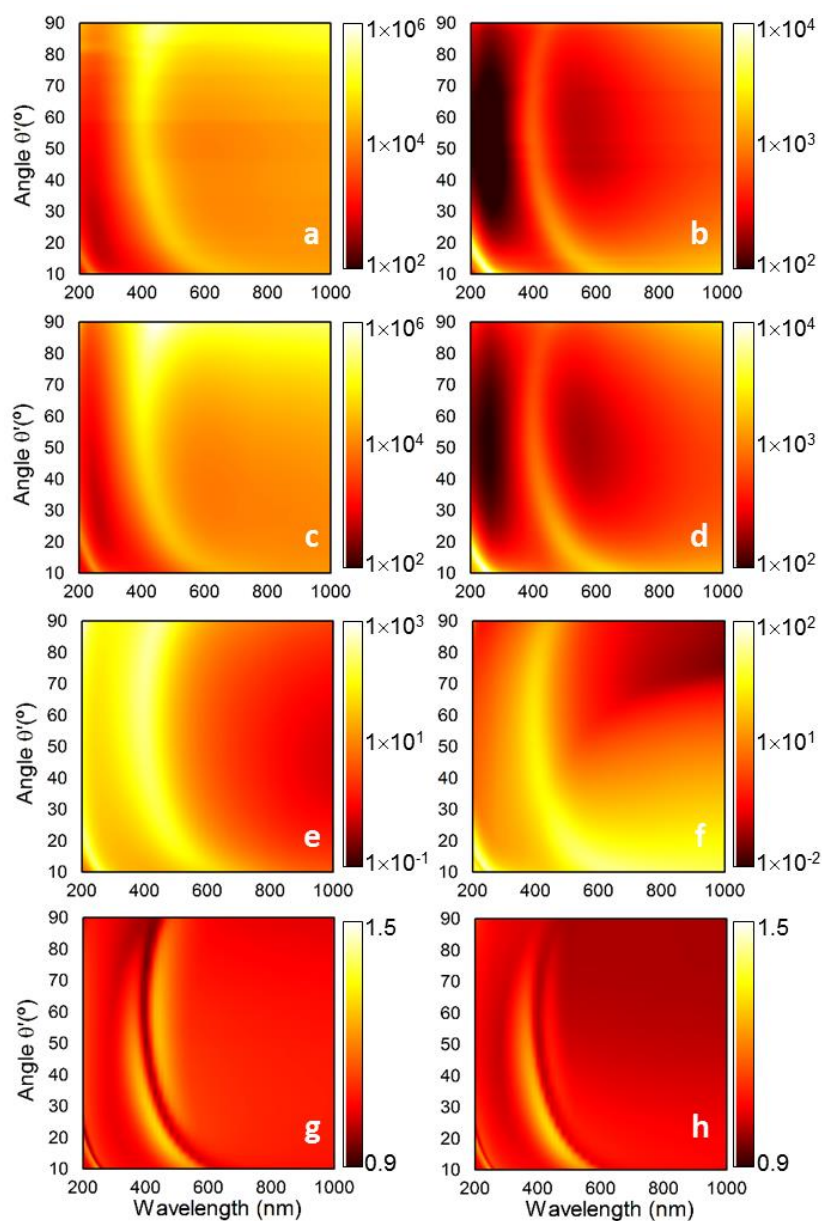**Nonradiative, radiative and absorption cross section.**

Figure S4. Analytical (a, b) and numerical (c, d) nonradiative Purcell enhancement, along with the numerical radiative Purcell spectra (e, f) and absorption cross section (g, h), for 8 nm long arm tripods with varying θ' under vertical (first column) and horizontal dipole (second column) excitation [plane-wave excitation for (g, h)]. The contourplots in panles a-f are in logarithmic color scale. On the contrary, the contour plots in panels g and h are in linear scale to better appreciate the results.

11

Changing orientation of the nanoemitter - $\theta' = 10^o$
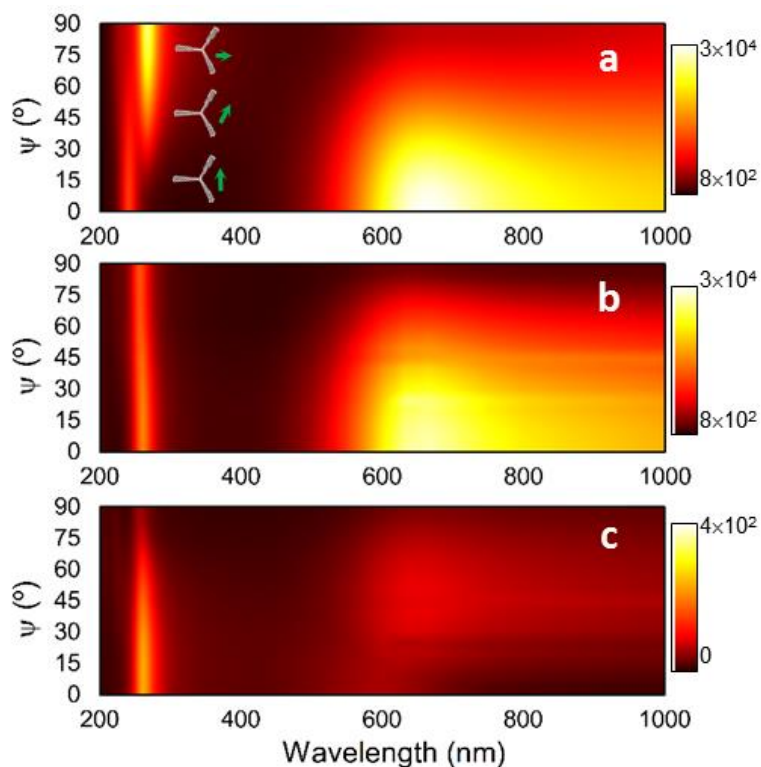
Figure S5. Analytical (a) and simulation (b) results of the nonradiative Purcell enhancement along with the radiative spectra (c) for an Al nanotripod with $\theta' = 10^o$ illuminated by a dipole source with different orientations ranging from 0 to 90°. The contour plots are in linear scale to better appreciate the results.
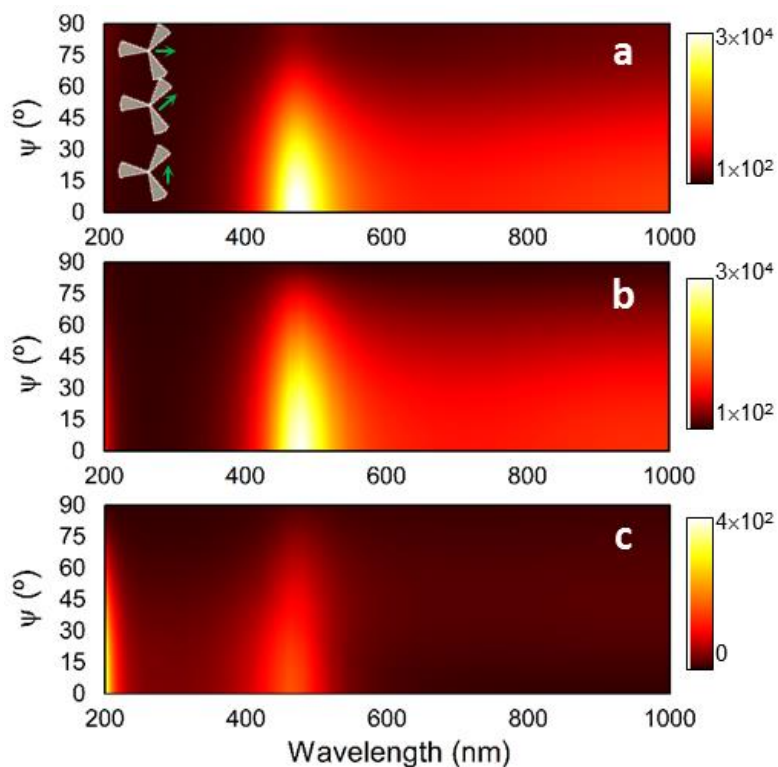
Changing orientation of the nanoemitter - $\theta' = 25^o$

Figure S6. Analytical (a) and simulation (b) results of the nonradiative Purcell enhancement along with the radiative spectra (c) for an Al nanotripod with $\theta' = 25^o$ (and touching arms) illuminated by a dipole source with different orientations ranging from 0 to 90°. The contour plots are in linear scale to better appreciate the results.

Rotating the Al nanotripod - $\theta' = 10^o$
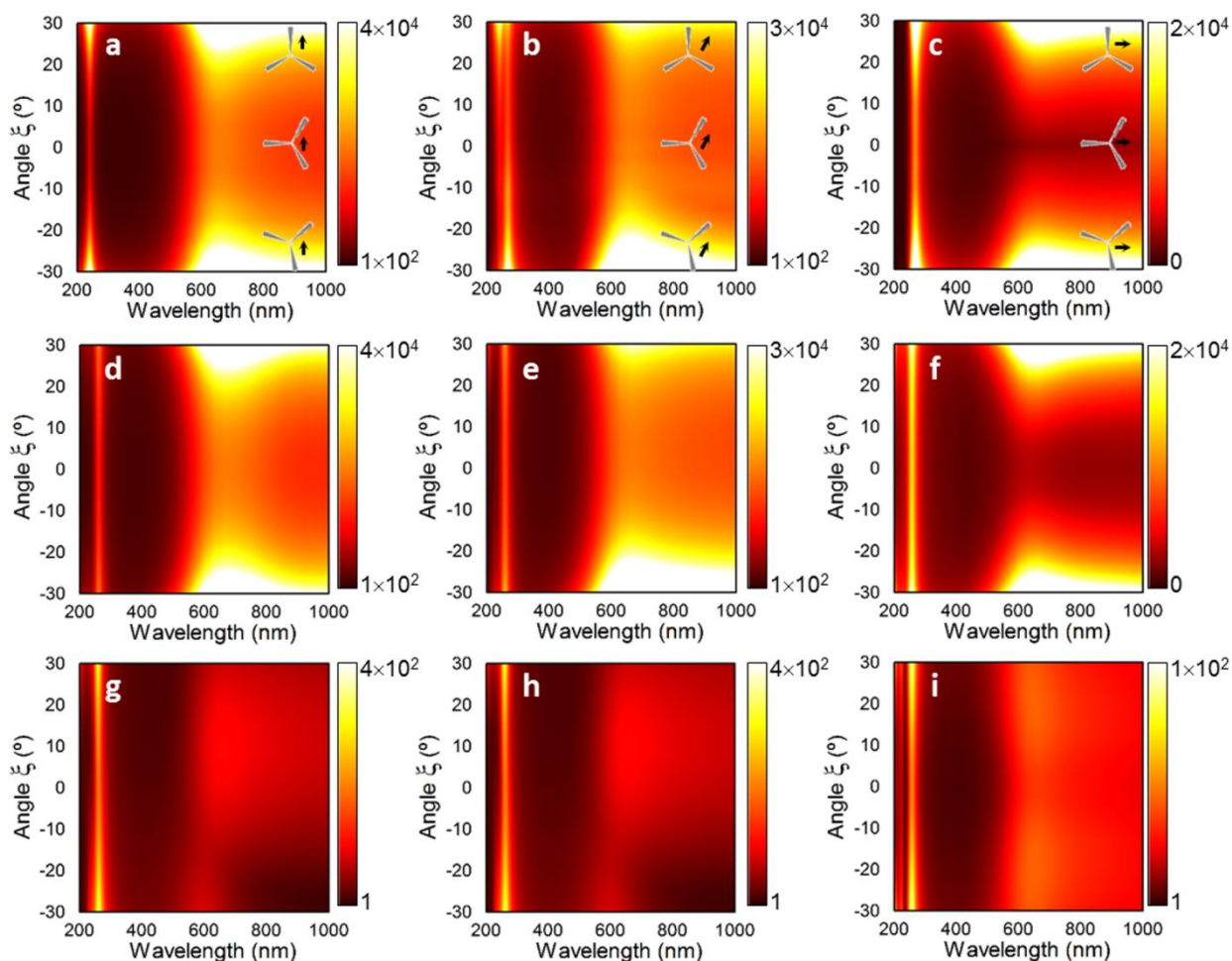
Figure S7. Analytical (first row) and numerical (second row) results of the nonradiative Purcell enhancement, along with the radiative spectra (third row) for a nanotripod with $\theta' = 10^o$ (and touching arms), when it is rotated from -30° to 30°. The tripods are excited by a point dipole with orientation: vertical (first column), 45° (second column), and horizontal (third column). The contour plots are in linear scale to better appreciate the results.
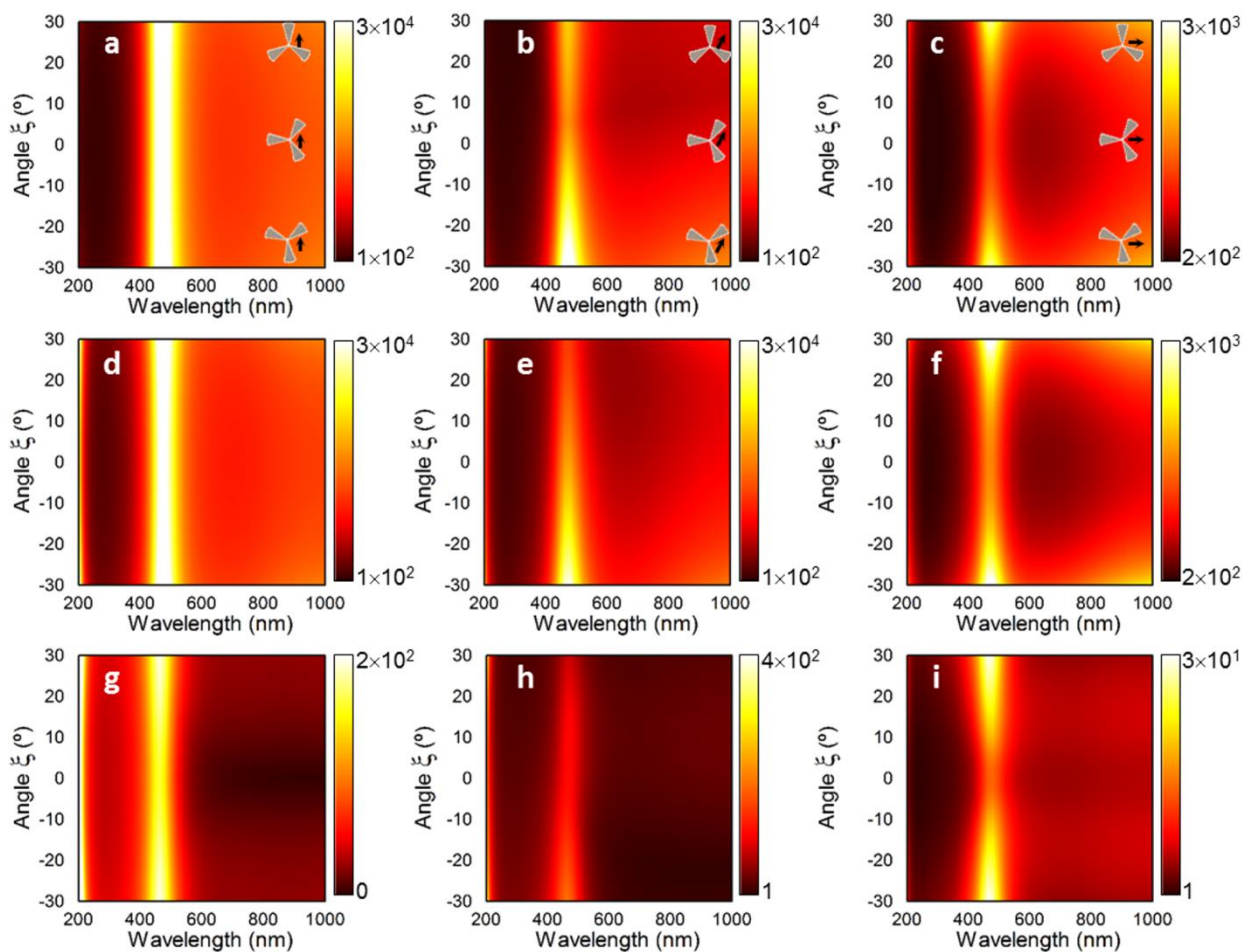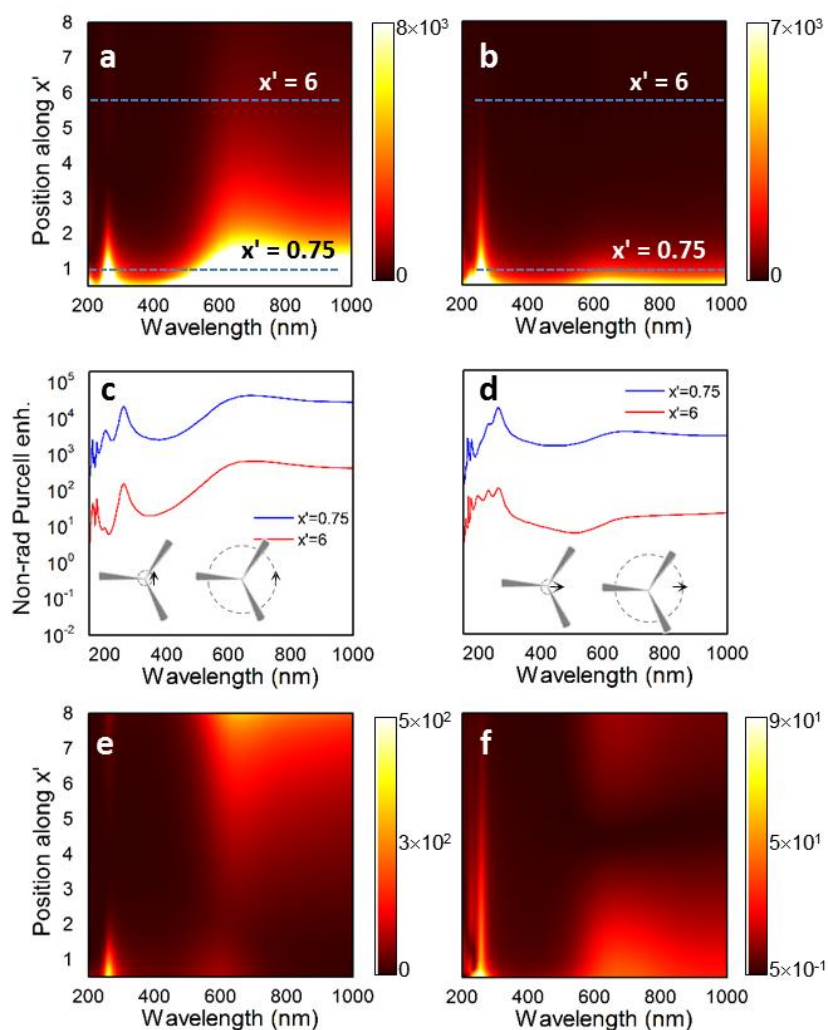
Rotating the Al nanotripod - $\theta' = 25^{\circ}$

Figure S8. Analytical (first row) and numerical (second row) results of the nonradiative Purcell enhancement, along with the radiative spectra (third row) for a nanotripod with $\theta' = 25^{\circ}$ (and touching arms), when it is rotated from -30° to 30°. The tripods are excited by a point dipole with orientation: vertical (first column), 45° (second column), and horizontal (third column). The contour plots are in linear scale to better appreciate the results.

Moving the dipole along the *x'*- axis - *θ' = 10°*

Figure S9. Simulation results of the nonradiative Purcell enhancement (first row) along with the radiative spectra (third row) for a nanotripod with *θ' = 10°* and touching arms. The dipole source is displaced along the *x'* axis from 0.5 to 8 nm for different emitter orientations: vertical (first column), horizontal (second column). The contour plots are in linear scale to better appreciate the results. The panels in the second row show the nonradiative Purcell enhancement extracted from panels (a, b) for *x' = 0.75* nm and *x' = 6* nm for vertical (c) and horizontal (d) orientation.
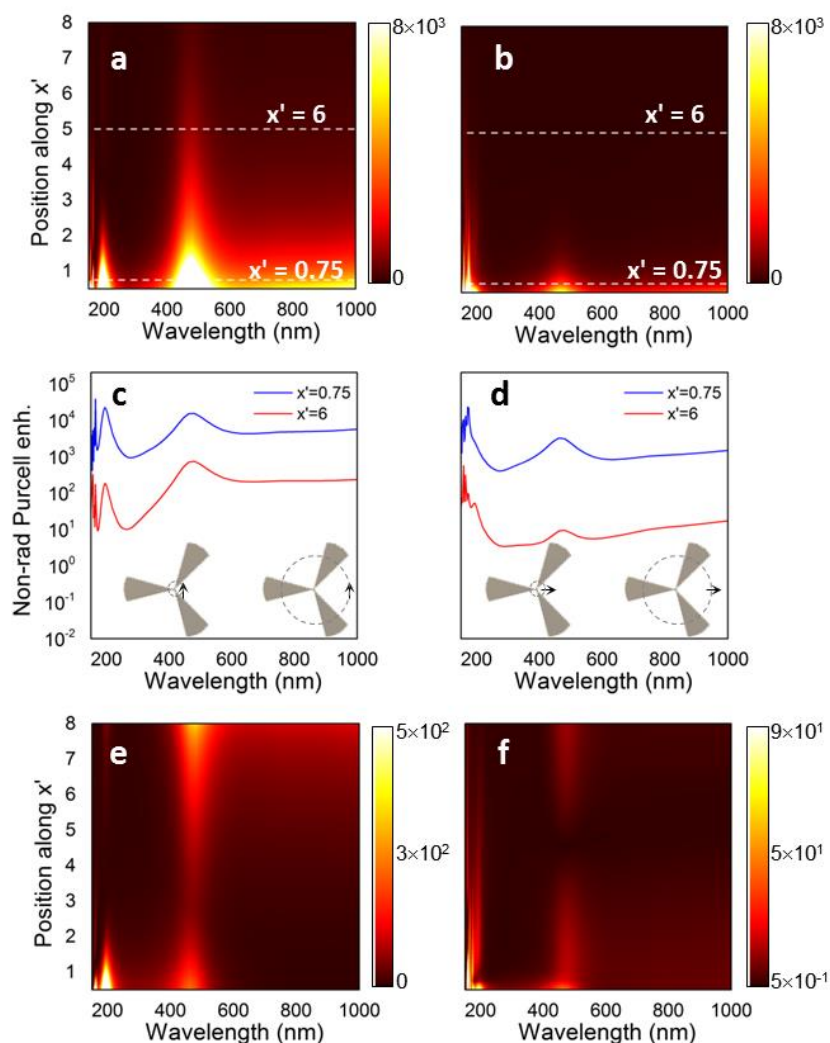
Moving the dipole along the *x'*- axis - *θ' = 25°*

Figure S10. Simulation results of the nonradiative Purcell enhancement (first row) along with the radiative Purcell spectra (third row) for a nanotripod with *θ' = 25°* and touching arms. The dipole source is displaced along the *x'* axis from 0.5 to 8 nm for different emitter orientations: vertical (first column), horizontal (second column). The contour plots are in linear scale to better appreciate the results. The panels in the second row show the nonradiative Purcell enhancement extracted from panels (a, b) for *x' = 0.75* nm and *x' = 6* nm for vertical (c) and horizontal (d) orientation.

Phase correction under vertical and horizontal dipole

The calculation of $\Delta\varphi_1$ and $\Delta\varphi_2$ is done by fitting the analytically-computed wavelength of the fundamental mode ($n = 1$ LSP mode) to the simulations.
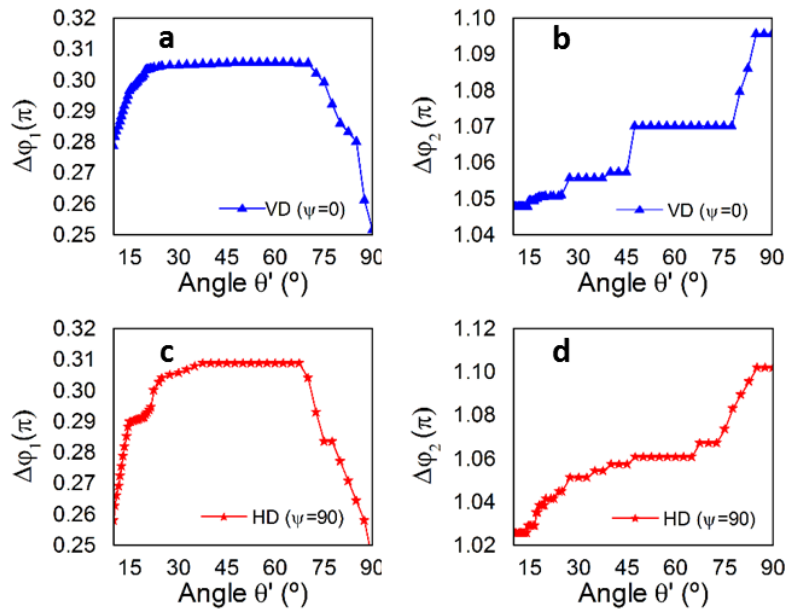

Figure S11. Phase correction $\Delta\varphi_1$ (first column) and $\Delta\varphi_2$ (second column) as a function of θ' when a vertical (first row) and horizontal (second row) dipole is used.

The methodology is as follows: the gapped (disconnected) nanotripod (nanotrimer) is studied first; since such nanotrimer has only open-ended edges, it only requires the estimation of one phase correction $\Delta\varphi$; since $\Delta\varphi$ is the only unknown, it is extracted then by fitting the analytical to the numerically-computed wavelength of the nanotrimer fundamental LSP mode.[1] This $\Delta\varphi$ from the nanotrimer corresponds to $\Delta\varphi_1$ (i.e., the complex reflection at the open-ended edge) for the nanotripod. Hence, again for the nanotripod, we are left with just one unknown $\Delta\varphi_2$ (accounting for the complex reflection at the comb base) that is estimated

[1] V. Pacheco-Peña, M. Beruete, A. I. Fernández-Domínguez, Y. Luo, and M. Navarro-Cía, *ACS Photonics* **3**, 1223-1232 (2016).

by fitting the analytical to the numerically-computed wavelength of the nanotripod

fundamental LSP mode.

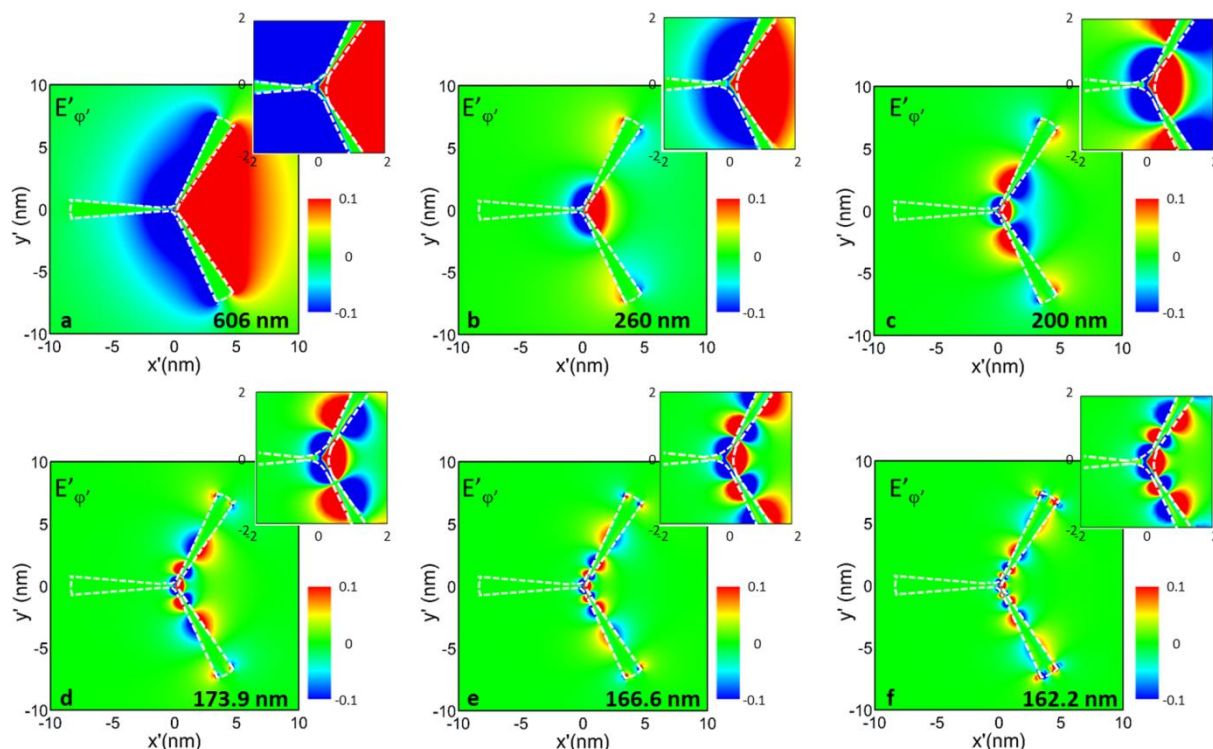**Field distribution for vertical dipole placed at *x'* = 0.75 nm - *θ'* = 10°**

Figure S12. Snapshot of the E'$_{\varphi'}$ field for a tripod nanoantenna with *θ'* = 10° excited with a vertically oriented dipole placed at *x'* = 0.75 nm. The field distributions are evaluated at the nonradiative Purcell enhancement peaks found in Fig. S9c. The inset of each panel shows a zoom-in of the field distribution at the center of the nanotripod. Note that the color scale has been saturated from −0.1 to 0.1 in order to better appreciate the field distribution.

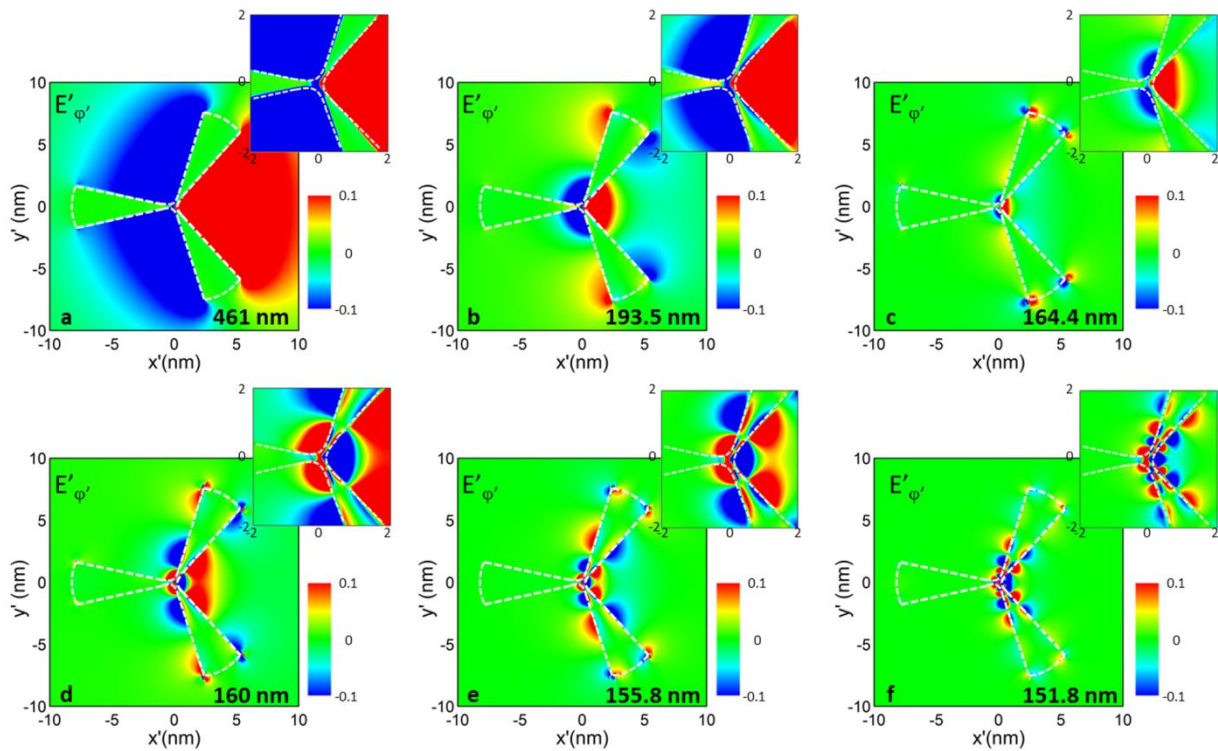**Field distribution for a vertical dipole placed at *x' = 0.75 nm - θ' = 25°***

Figure S13. Snapshot of the E'_φ' field for a tripod nanoantenna with *θ' = 25°* excited with a vertically oriented dipole placed at *x' = 0.75* nm. The field distributions are evaluated at the nonradiative Purcell enhancement peaks found in Fig. S10c. The inset of each panel shows a zoom-in of the field distribution at the center of the nanotripod. Note that the color scale has been saturated from −0.1 to 0.1 in order to better appreciate the field distribution.

Field distribution for a horizontal dipole placed at *x'* = 0.75 nm - *θ'* = 10⁰

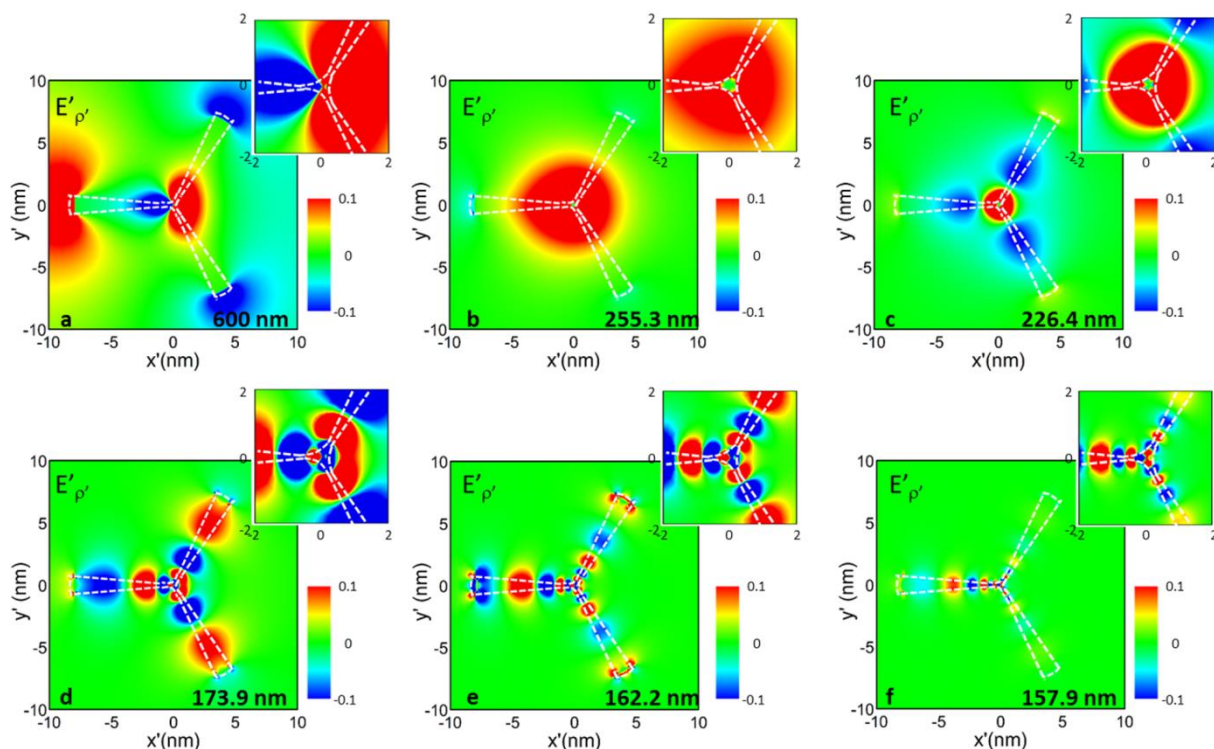**Figure S14.** Snapshot of the E'$_{\rho'}$ field for a tripod nanoantenna with *θ'* = 25⁰ excited with a horizontally oriented dipole placed at *x'* = 0.75 nm. The field distributions are evaluated at the nonradiative Purcell enhancement peaks in Fig. S10d. The inset of each panel shows a zoom-in of the field distribution at the center of the nanotripod. Note that the color scale has been saturated from -0.1 to 0.1 in order to better appreciate the field distribution.

Field distribution for a horizontal dipole placed at *x'* = 0.75 nm - *θ'* = 25°

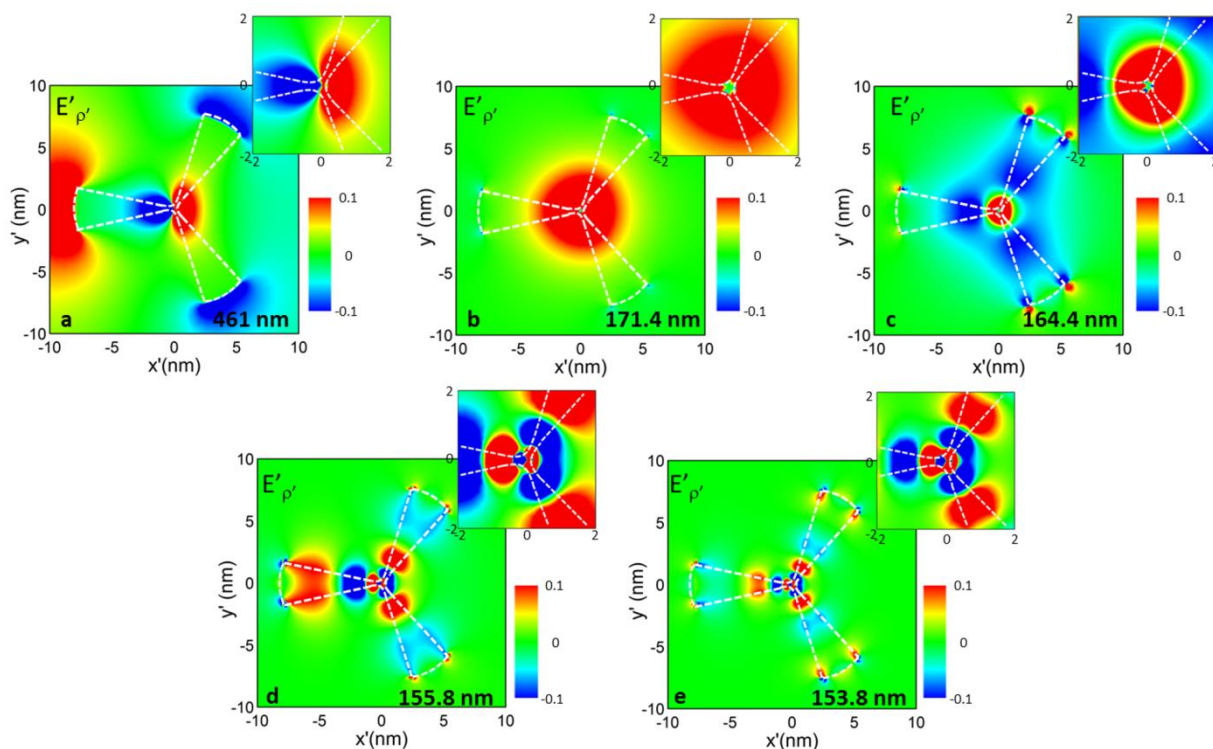**Figure S15.** Snapshot of the E'$_{\rho'}$ field for a tripod nanoantenna with *θ'* = 25° excited with a horizontally oriented dipole placed at *x'* = 0.75 nm. The field distributions are evaluated at the nonradiative Purcell enhancement peaks in Fig. S10d. The inset of each panel shows a zoom-in of the field distribution at the center of the nanotripod. Note that the color scale has been saturated from -0.1 to 0.1 in order to better appreciate the field distribution.